CHEMISTRY OF MATERIALS

ARTICLE

pubs.acs.org/cm

Composition-Controlled Synthesis of Bimetallic PdPt Nanoparticles and Their Electro-oxidation of Methanol

Yi Liu,[†] Miaofang Chi,[‡] Vismadeb Mazumder,[†] Karren L. More,[‡] Stuart Soled,[§] Juan D. Henao,[§] and Shouheng Sun*[,†]

[†]Department of Chemistry, Brown University, Providence, Rhode Island 02912, United States

[‡]Oak Ridge National Laboratory (ORNL), Oak Ridge, Tennessee 37831, United States

[§]ExxonMobil Research and Engineering Co., Annandale, New Jersey 08801, United States

Supporting Information

ABSTRACT: PdPt alloy nanoparticles (NPs) are promising catalysts for various chemical reactions because of the presence of powerful catalytic components of Pt and Pd on the surface of one nanostructure. In this paper, we report a facile synthesis of polyhedral PdPt alloy NPs via coreduction of $Pd(acac)_2$ (acac = acetylacetonate) and $Pt(acac)_2$ with morpholine borane in oleylamine at 90 and 180 °C. In the synthesis, the molar ratio of the two metal precursors added in the reaction mixture was carried over to the final PdPt NP product, and compositions of the PdPt NPs were readily tuned from $Pd_{88}Pt_{12}$ to $Pd_{34}Pt_{66}$. These PdPt NPs show the composition-dependent catalytic activity for methanol oxidation, with NPs in 40−60 atomic % Pt exhibiting the superior activity and durability.

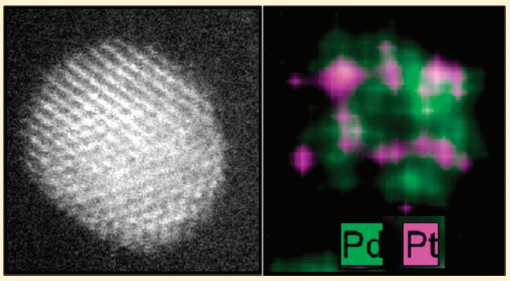

KEYWORDS: palladium platinum alloy, bimetallic nanoparticles, methanol oxidation

INTRODUCTION

Synthesis of bimetallic alloy nanoparticles (NPs) with controlled size, shape, and composition is key to the development of advanced nanocatalysts for various chemical reactions.[1−4] Among all Pt-based bimetallic NPs studied,[1−7] PdPt alloy NPs are especially attractive for catalyzing multiple reactions as the result of the presence of the powerful catalytic components of Pt and Pd. Recent studies have indicated that PdPt alloy NPs are promising catalysts for hydrogenation of aromatic hydrocarbons and for electro-oxidation of small organic molecules with high sulfur[8,9] and CO tolerance.[10,11] PdPt NPs are commonly made by an impregnation method in which Pd and Pt precursors are absorbed on the solid supporting materials and chemically reduced.[12,13] High quality solid or hollow PdPt nanocubes were also prepared by the coreduction of $PdCl_2$ and K_2PtCl_6 in the presence of sodium lauryl sulfate, KBr, and polyvinylpyrrolidone (PVP)[14] or by a sequential reduction of $Pd(acac)_2$ (acac = acetylacetonate) and $Pt(acac)_2$ in the presence of PVP and NaI through galvanic replacement of Pd(0) NPs and $Pt(acac)_2$.[15] Similar approaches also led to the formation of PdPt nanocubes,[16] nanodendrites,[17,18] tetrahedrons,[16] concave nanocubes,[19] star-shaped decahedrons, and triangular nanoplates.[20] Despite these efforts, PdPt NPs synthesized from these previous methods lack either size (for impregnation method) or composition tunability over a wide range (for solution phase synthesis), and they are generally not suitable for composition-dependent catalytic studies.

Here, we report an improved synthesis of polyhedral PdPt alloy NPs with controls on sizes (3.5−6.5 nm) and compositions ($Pd_{88}Pt_{12}$ to $Pd_{34}Pt_{66}$). We developed a convenient way for making monodisperse Pd NPs via the reduction of $Pd(acac)_2$ with *tert*-butylamine borane in oleylamine (OAm).[21] By adjusting the reducing power of the amine borane complex, we could control the nucleation and growth of Pd and Pt and make uniform PdPt alloy NPs by reducing $Pd(acac)_2$ and $Pt(acac)_2$ with morpholine borane (MB) in OAm at 90 and 180 °C. These PdPt NPs were active catalyst for methanol oxidation reaction (MOR) in $HClO_4$ solution, and their activity was composition-dependent. The PdPt alloy NPs with Pt in 40−60 atomic % showed higher activity and durability than either Pd NPs or the commercial BASF Pt catalyst. Our study indicates that, once made with a wide range of composition control, these PdPt alloy NPs can serve as an excellent platform for studying cocatalysis effects of Pd and Pt and for studying catalysis optimization.

EXPERIMENTAL SECTION

Chemicals. Palladium(II) acetylacetonate, $Pd(acac)_2$, (99%, Strem Chemicals), platinum(II) acetylacetonate, $Pt(acac)_2$, (97%, Aldrich), morpholine borane (MB, 95%, Aldrich), oleylamine (OAm, technical grade, 70%, Aldrich), carbon black (Kejen EC 600J), acetic acid (ACS reagent, ≥99.7%, Sigma-Aldrich), commercial Pt catalyst (BASF, 46% loading), perchloric acid (70−72%, J. T. Baker), and methanol

Received: May 25, 2011
Revised: July 5, 2011
Published: August 19, 2011

(≥99.8%, Mallinckrodt Chemicals) were purchased and used as received.

Synthesis of PdPt NPs. Under a nitrogen gas (N_2) flow and magnetic stirring, $Pd(acac)_2$ and $Pt(acac)_2$ were dissolved in 15 mL of OAm at room temperature and heated to 60 °C. In a glass vial, 0.2 g of MB was dissolved in 3 mL of OAm, and the mixture was quickly injected into the 60 °C precursor solution to initiate the burst nucleation. Then, the temperature was raised to 90 °C, and the mixture was kept at this temperature for 30 min. For Pd NP and $Pd_{88}Pt_{12}$ NP growth, the reaction was ceased after 30 min of heating. For other PdPt NPs, the reaction mixture was further heated to 180 °C and kept at 180 °C for 30 min. After the mixture had cooled to room temperature, the PdPt NPs were separated by adding isopropanol and centrifugation. The PdPt NPs were further washed several times by a mixture of hexane and isopropanol and, finally, were dispersed in hexane. The Pd/Pt atomic ratio was controlled by the Pd and Pt precursor ratios. The Pd, $Pd_{88}Pt_{12}$, $Pd_{67}Pt_{33}$, $Pd_{52}Pt_{48}$, and $Pd_{34}Pt_{66}$ NPs were synthesized by using 0.25 mmol of $Pd(acac)_2$ and 0.05, 0.125, 0.25, or 0.50 mmol of $Pt(acac)_2$.

Preparation of the Carbon Supported Pd or PdPt NPs (PdPt/C) Catalysts. NPs (10 mg) in hexane (15 mL) were mixed with 10 mg of carbon black (Ketjen EC-600J) and sonicated for 1 h to load all the NPs on carbon. The PdPt/C was separated by centrifugation and then heated in acetic acid at 70 °C for 12 h to clean the NP surface as reported.[21] Then, the PdPt/C was separated from the acetic acid and washed with ethanol three times. Finally, the PdPt/C was dried under a gentle flow of nitrogen and suspended in deionized (DI) water by sonication to form a 2 mg/mL PdPt/C suspension. The commercial BASF Pt (46% Pt loading) was used without any treatment and was sonicated with water to form a 2 mg/mL BASF Pt catalyst suspension.

Electrochemical Measurement. PdPt/C water suspension (20 μL) was deposited on a glassy carbon rotating disk electrode (5 mm in diameter, mirror polished) and dried under vacuum at room temperature. Nafion water solution (10 μL, 0.1 wt %) was deposited over the NPs, and the solvent was evaporated. Ag/AgCl and Pt wire were used as the reference electrode and counter electrode, respectively. The electrodes were immersed in the nitrogen saturated 0.1 M $HClO_4$ solution (25 °C), and the potential was scanned from −0.25 to 1.0 V at a scan rate of 50 mV/s. The scan was repeated several times to ensure that a stable cyclic voltammetry (CV) was obtained. The CVs were used to estimate the electrochemical active surface area (ECASA) of the catalyst by calculating the hydrogen under potential desorption (H_{upd}) area of the catalyst. CVs for MOR were conducted in 0.1 M $HClO_4$ and 0.1 M methanol from 0 to 0.9 V at a scan rate of 50 mV/s. The stability was tested by chronoamperometry at 0.5 V in 0.1 M $HClO_4$ and 0.1 or 1 M methanol for 1 h.

Characterization. Transmission electron microscopy (TEM) and high resolution TEM (HRTEM) images were acquired on a Philips/FEI CM 20 (200 kV) and a JEOL 2010 transmission electron microscope. The high-angle annular dark-field scanning TEM (HAADF-STEM) image and elemental mapping were obtained on an aberration corrected JEOL 2200FS microscope with beam size ~ 0.8 Å for imaging and beam size ~ 2 Å for chemical analysis. X-ray diffraction (XRD) patterns of the samples were recorded on a Bruker AXS D8-Advanced diffractometer with Cu Kα radiation (λ = 1.5418 Å). The compositions of the samples were measured by inductively coupled plasma−atomic emission spectroscopy (ICP-AES). Electrochemical measurements were performed on a Pine Electrochemical Analyzer, model AFCBP1.

RESULTS AND DISCUSSION

The PdPt NPs were synthesized by the controlled reduction of $Pd(acac)_2$ and $Pt(acac)_2$ in OAm, as described in the Experimental Section. In the synthesis, $Pd(acac)_2$ and $Pt(acac)_2$ were dissolved in OAm at room temperature. The pale yellow solution was then heated to 60 °C. The MB in OAm solution was quickly injected into this 60 °C solution to initiate the burst nucleation, which was indicated by the solution color change from pale yellow to black seconds after the MB injection. The solution was further heated to higher temperatures to complete the NP growth. Figure 1a shows a typical TEM image of the monodisperse 5 nm $Pd_{67}Pt_{33}$ NPs. Under similar reaction conditions, 5.5 nm Pd NPs, 5 nm $Pd_{88}Pt_{12}$ NPs, 3.5 nm $Pd_{52}Pt_{48}$ NPs, and 3.5 nm $Pd_{34}Pt_{66}$ NPs were also made (Figure S1 in the Supporting Information). Figure 1b shows the high resolution aberration-corrected HAADF-STEM and bright field images of a typical $Pd_{67}Pt_{33}$ NP with the crystal fringe measured to be ~0.23 nm, corresponding to the (111) interplanar spacing of the face-centered cubic (fcc) alloy structure. The alloy formation was further characterized by elemental mapping. Figure 1c shows the HAADF-STEM image of several representative $Pd_{67}Pt_{33}$ NPs and the related mapping with Pd (green) and Pt (red). Despite the limited sensitivity of the mapping technique, the color distribution within each NP indicates that the alloy structure is formed indeed in each NP. The alloy formation in the $Pd_{34}Pt_{66}$ NPs was also confirmed by the HAADF-STEM and elemental mapping analyses (Figure S2 in the Supporting Information).

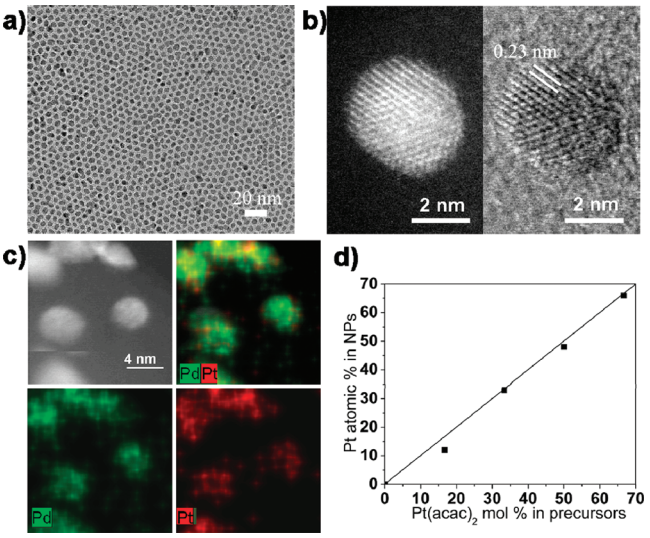

Figure 1. (a) TEM image of the 5 nm $Pd_{67}Pt_{33}$ NPs. (b) High resolution HAADF-STEM image (left) and bright field image (right) of a single $Pd_{67}Pt_{33}$ NP. (c) HAADF-STEM image and the corresponding elemental map of several representative 5 nm $Pd_{67}Pt_{33}$ NPs. (d) Correlation between the amount of $Pt(acac)_2$ added and the amount of Pt obtained in the final PdPt NP product.

The composition of the PdPt NPs was tuned by the amounts of $Pd(acac)_2$ and $Pt(acac)_2$ added in the synthesis, and it was measured by ICP-AES. Figure 1d shows a plot of atomic % of Pt in PdPt NPs vs mol % of $Pt(acac)_2$ added in the reaction mixture containing 0.25 mmol $Pd(acac)_2$. The linear relationship with a slope of nearly one indicates that the molar ratio of the two metal precursors is carried over to the final PdPt NP product.

Furthermore, at a constant composition, the size of the PdPt NPs was tuned by varying the MB injection temperature. For example, injecting MB at 40, 60, and 80 °C led to the formation of 6.5, 5, and 4.5 nm $Pd_{67}Pt_{33}$ NPs, respectively (Figures 1a and 2). In the synthesis, the color of the reaction solution was changed from pale yellow to black in about 15, 7, and 5 s after MB injection at 40, 60, and 80 °C, respectively. These indicate that a lower

dx.doi.org/10.1021/cm2014785 |Chem. Mater. 2011, 23, 4199–4203

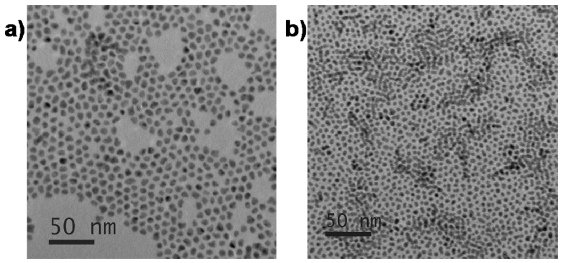

Figure 2. TEM images of (a) 6.5 nm and (b) 4.5 nm $Pd_{67}Pt_{31}$ NPs, synthesized by MB injection at 40 and 80 °C.

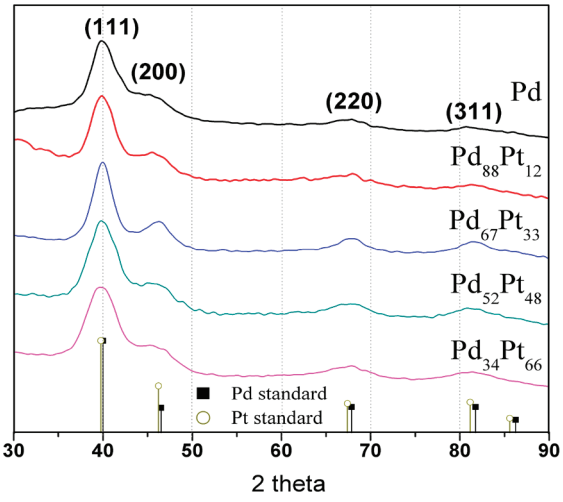

Figure 3. XRD patterns of Pd, $Pd_{88}Pt_{12}$, $Pd_{67}Pt_{33}$, $Pd_{52}Pt_{48}$, and $Pd_{34}Pt_{66}$ NPs. The drop-lines are the standard peaks for Pd (■) and Pt (○).

temperature injection resulted in slower reduction and the formation of fewer seeds. The subsequently increased temperature enabled continuous reduction of the rest of the Pd and Pt precursors by excess MB, leading to larger NPs. In our current synthetic conditions, OAm can only protect Pd NPs from aggregation at temperatures below 90 °C. Therefore, 90 °C was the maximum temperature used for Pd NP and Pd-rich $Pd_{88}Pt_{12}$ NP synthesis. However, in the presence of more Pt, PdPt NPs can be stabilized by OAm at temperatures up to 180 °C.

The XRD pattern (Figure 3) was used to characterize the structure of the as synthesized Pd and PdPt NPs. All NPs show four diffraction peaks corresponding to (111), (200), (220), and (311) of the fcc structure. The crystalline sizes of the NPs can be estimated from the (111) peak broadening using Scherrer's formula: 2.56, 2.98, 3.27, 2.27, and 2.16 nm for Pd, $Pd_{88}Pt_{12}$, $Pd_{67}Pt_{33}$, $Pd_{52}Pt_{48}$, and $Pd_{34}Pt_{66}$ NPs, respectively. They are smaller than the physical dimensions of the related NPs measured from the TEM images, indicating that small crystalline domains are present within one NP.

The PdPt alloy structures were further characterized by their composition-dependent electrochemical behaviors. To perform electrochemical studies, 10 mg of the as prepared PdPt NPs were loaded onto 10 mg of carbon black (Kejen EC600J) followed by acetic acid cleaning at 70 °C for 12 h.[21] Figure 4a and Figure S3a (in the Supporting Information) are representative TEM and HAADF-STEM images of the PdPt NPs/C after this acetic acid treatment. There was no observable morphology change or

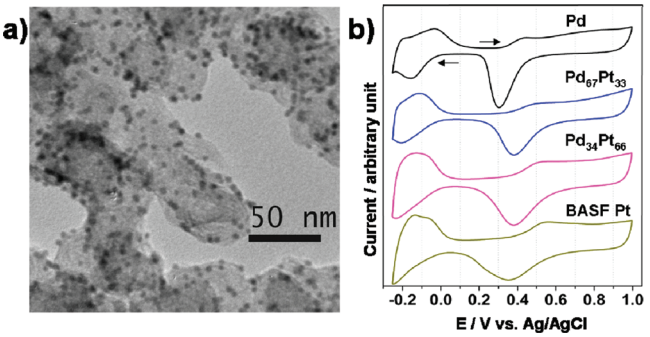

Figure 4. (a) TEM image of the $Pd_{52}Pt_{48}$ NPs loaded on carbon black after acetic acid treatment. (b) CVs of the Pd, $Pd_{67}Pt_{33}$, and $Pd_{34}Pt_{66}$ NPs/C and BASF Pt NP catalysts obtained in the deaerated 0.1 M $HClO_4$.

aggregation. The PdPt NPs/C was further dispersed in water to make a 2 mg/mL suspension, and a 20 μL catalyst sample was loaded onto the electrode and, after water evaporation, fixed with Nafion. Cyclic voltammetries (CV) of the Pd, PdPt NPs/C, and BASF Pt (2−3 nm Pt NPs (46 wt %) loaded on carbon black, as shown in Figure S3b in the Supporting Information) in the deaerated 0.1 M $HClO_4$ are shown in Figure 4b and Figure S4 (in the Supporting Information). In each CV, the potential was scanned positively from −0.25 to 1.0 V and then negatively to −0.25 V. In the positive scanning direction, hydrogen under potential desorption (H_{upd}) on the NP surface is first observed as a broad peak. The second peak indicates the formation of a hydroxide layer (OH_{ad}) on the NP surface. In the negative scanning direction, the two peaks are attributed to NP surface reduction and hydrogen adsorption, respectively. We can see that the H_{upd} peaks of the PdPt NPs are located between those from the pure Pd and Pt and have a negative shift when the Pt component is increased. A similar trend was observed for the OH_{ad} peaks. Pd−OH_{ad} is formed at a lower potential than Pt−OH_{ad} because Pd is more vulnerable to oxidation. This confirms that Pd and Pt are tightly associated with each other in the PdPt structure and PdPt NPs have an alloy, not a core/shell structure, as in Au/Pt[4] and Au/$FePt_3$,[22] where the related redox peak does not shift.

The PdPt NPs show much enhanced catalysis for MOR than both BASF Pt and Pd NPs/C catalysts, and their activity is Pd/Pt composition-dependent. From the H_{upd} area in the CV curves (Figure 4b and Figure S4 in the Supporting Information), the electrochemically active surface area (ECASA) of the catalysts can be estimated (see the Supporting Information)[23] to be 8.91, 7.66, 8.13, 9.59, 10.4, and 12.8 cm^2 for Pd, $Pd_{88}Pt_{12}$, $Pd_{67}Pt_{33}$, $Pd_{52}Pt_{48}$, and $Pd_{34}Pt_{66}$ NPs/C and BASF Pt, respectively. The specific ECASAs (the ECASA per unit weight of metal) were estimated from the ECASA and the amount of metal loaded on the electrode and were found to be 51, 44, 46, 54, 59, and 70 m^2/g metal (metal = Pd, Pd + Pt, or Pt). The Pd and PdPt alloy NPs, as a result of their larger NP sizes, have smaller specific ECASAs than the BASF Pt. The catalytic activity for each type of the NP catalyst was evaluated by the current density (J) (normalized with the ECASA) generated from the MOR vs potential applied. The $J-V$ curves related to the MOR for the Pd, $Pd_{67}Pt_{33}$, $Pd_{34}Pt_{66}$, and BASF Pt catalysts in 0.1 M methanol are shown in Figure 5a. In obtaining these curves, the potentials were scanned from 0 to 0.9 V and then back to 0 V. In the forward scan, the current density first increases as higher potential promotes the MOR until the NP's surface is oxidized, resulting in a drop of

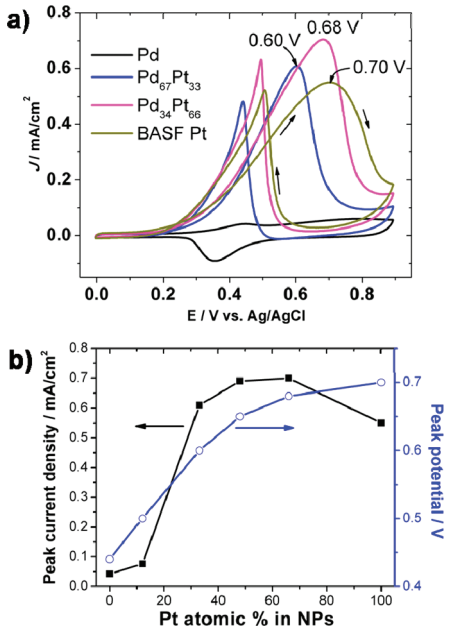

Figure 5. (a) $J-V$ curves reflecting MOR catalysis of NP catalysts in 0.1 M $HClO_4$ and 0.1 M methanol. (b) Methanol oxidation peak current density and peak potential vs the Pt atomic % in PdPt NPs.

current density. In the backward scan, as the oxidized surface is reduced, the catalyst regains its activity, leading to a current density jump. From Figure 5a, as well as Figure S5 (in the Supporting Information), we can see that Pd is the least active catalyst for MOR in $HClO_4$. In the same test conditions, $Pd_{88}Pt_{12}$ NPs are slightly more active and $Pd_{52}Pt_{48}$, $Pd_{67}Pt_{33}$, and $Pd_{34}Pt_{66}$ NPs are much more active than Pd NPs. From the figures, we can also see that both peak potentials and current densities related to MOR change with the increase in Pt content. The plot of these peak potentials and peak current densities vs Pt atomic % in NPs (Figure 5b) shows a "maximum activity plateau" for catalysts having 40−60% [Pt]. Similar composition-dependent MOR activity is also observed in the $J-V$ curves normalized against Pt weight (Figure S6 in the Supporting Information).

The MOR activity of the PdPt NPs can be explained by the bifunctional methanol oxidation mechanism:[11] Pd is mainly responsible for the water dehydrogenation to form Pd−OH, while Pt catalyzes the methanol dehydrogenation to form Pt−CO. The reaction between Pd−OH and Pt−CO produces CO_2 and regains the active metal surface. Without Pd, the water dehydrogenation on Pt occurs at a higher potential, making the overall oxidation process on pure Pt sluggish. The activity also decreases with the presence of excessive Pd as a result of the lack of Pt for methanol dehydrogenation, as seen in the MOR catalysis of Pd and $Pd_{88}Pt_{12}$ NPs.

Stability of the PdPt NPs for MOR was also studied via a chronoamperometric approach. Pt NP catalysts are known to deteriorate quickly in the oxidizing acidic environment.[24] Bimetallic NPs have been shown to be a possible solution.[25] The stability of the PdPt NPs was tested by the 1 h chronoamperometric test at a constant potential of 0.5 V in 0.1 M $HClO_4$ with 0.1 M methanol, as shown in Figure 6 and Figure S7 (in the Supporting Information). $Pd_{52}Pt_{48}$ and $Pd_{34}Pt_{66}$ NPs have higher current density than the BASF Pt, at both the start and the end of the stability test. The chronoamperometric curves

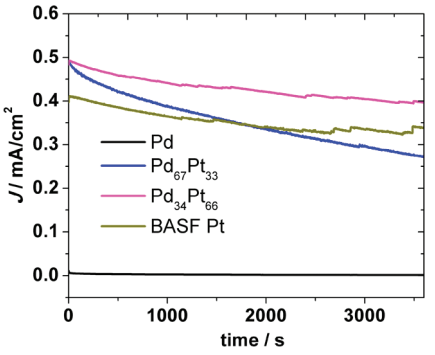

Figure 6. Chronoamperometric curves reflecting the stability of the NP catalysts in 0.1 M $HClO_4$ and 0.1 M methanol at constant voltage 0.5 V for 1 h.

(Figure S8 in the Supporting Information) with higher methanol concentration (1 M) were used to further distinguish the performance of $Pd_{67}Pt_{33}$, $Pd_{52}Pt_{48}$, and $Pd_{34}Pt_{66}$ NPs. Interestingly, in both concentration conditions, the $Pd_{34}Pt_{66}$ NPs have the least performance decay. As Pd NPs tend to lose their ECASA as a result of their aggregation,[21] higher [Pd] content in $Pd_{67}Pt_{33}$ and $Pd_{52}Pt_{48}$ NPs might also induce faster activity decay. This is also the reason why the initial current density, $Pd_{52}Pt_{48}$ NPs ∼ 0.42 mA/cm^2, was reduced to $Pd_{52}Pt_{48}$ NPs ∼ 0.31 mA/cm^2 after the 1 h stability test (Figure S8). Our tests further confirm that, to achieve both activity and long-term stability for MOR, it is necessary to incorporate an acid-stable component into the PdPt system.[26]

CONCLUSION

In summary, we have reported a facile synthesis of monodisperse PdPt NPs by the morpholine borane reduction of $Pd(acac)_2$ and $Pt(acac)_2$ in oleylamine. The PdPt NPs have the alloy structure, with their compositions controlled from $Pd_{88}Pt_{12}$ to $Pd_{34}Pt_{66}$. These alloy NPs are more active and stable for MOR, and their activities are Pd/Pt composition-dependent, with Pt in 40−60% showing the optimum activity and stability. The reported PdPt NPs are not limited to catalyzing MOR but can be used for studying many other reactions as well. Work on exploring these bimetallic PdPt NPs for various chemical reactions, especially for the hydrogenation of aromatic compounds, is underway.

ASSOCIATED CONTENT

Supporting Information. Additional TEM, HRTEM, HAADF-STEM images, elemental mapping, and electrochemistry data. This material is available free of charge via the Internet at http://pubs.acs.org.

AUTHOR INFORMATION

Corresponding Author
*Fax: (+1) 401-863-9046. E-mail: ssun@brown.edu.

ACKNOWLEDGMENT

This work was supported by ExxonMobil Research and Engineering Co. Microscopy research supported in part by ORNL's Shared Research Equipment (SHaRE) User Facility,

which is sponsored by the Office of Basic Energy Sciences, U.S. Department of Energy.

REFERENCES

(1) Sun, S. H.; Murray, C. B.; Weller, D.; Folks, L.; Moser, A. *Science* **2000**, *287* (5460), 1989–1992.
(2) Ono, K.; Okuda, R.; Ishii, Y.; Kamimura, S.; Oshima, M. *J. Phys. Chem. B* **2003**, *107* (9), 1941–1942.
(3) Wang, C.; Peng, S.; Chan, R.; Sun, S. H. *Small* **2009**, *5* (5), 567–570.
(4) Xu, Z.; Carlton, C. E.; Allard, L. F.; Shao-Horn, Y.; Hamad-Schifferli, K. *J. Phys. Chem. Lett.* **2010**, *1* (17), 2514–2518.
(5) Wang, H. S.; Alden, L.; DiSalvo, F. J.; Abruna, H. D. *Phys. Chem. Chem. Phys.* **2008**, *10* (25), 3739–3751.
(6) Lee, Y. H.; Lee, G.; Shim, J. H.; Hwang, S.; Kwak, J.; Lee, K.; Song, H.; Park, J. T. *Chem. Mater.* **2006**, *18* (18), 4209–4211.
(7) Liu, Z.; Ada, E. T.; Shamsuzzoha, M.; Thompson, G. B.; Nikles, D. E. *Chem. Mater.* **2006**, *18* (20), 4946–4951.
(8) Yasuda, H.; Yoshimura, Y. *Catal. Lett.* **1997**, *46* (1), 43–48.
(9) Yoshimura, Y.; Toba, M.; Matsui, T.; Harada, M.; Ichihashi, Y.; Bando, K. K.; Yasuda, H.; Ishihara, H.; Morita, Y.; Kameoka, T. *Appl. Catal., A* **2007**, *322*, 152–171.
(10) Antolini, E. *Energy Environ. Sci.* **2009**, *2* (9), 915–931.
(11) Kua, J.; Goddard, W. A. *J. Am. Chem. Soc.* **1999**, *121* (47), 10928–10941.
(12) Zhang, H. X.; Wang, C.; Wang, J. Y.; Zhai, J. J.; Cai, W. B. *J. Phys. Chem. C* **2010**, *114* (14), 6446–6451.
(13) Li, H.; Sun, G.; Li, N.; Sun, S.; Su, D.; Xin, Q. *J. Phys. Chem. C* **2007**, *111* (15), 5605–5617.
(14) Yuan, Q.; Zhou, Z. Y.; Zhuang, J.; Wang, X. *Chem. Commun.* **2010**, *46* (9), 1491–1493.
(15) Huang, X. Q.; Zhang, H. H.; Guo, C. Y.; Zhou, Z. Y.; Zheng, N. F. *Angew. Chem., Int. Ed.* **2009**, *48* (26), 4808–4812.
(16) Yin, A.-X.; Min, X.-Q.; Zhang, Y.-W.; Yan, C.-H. *J. Am. Chem. Soc.* **2011**, *133* (11), 3816–3819.
(17) Wang, L.; Nemoto, Y.; Yamauchi, Y. *J. Am. Chem. Soc.* **2011**, *133* (25), 9674–9677.
(18) Wang, L.; Yamauchi, Y. *Chem.—Asian J.* **2010**, *5* (12), 2493–2498.
(19) Zhang, H.; Jin, M.; Wang, J.; Li, W.; Camargo, P. H. C.; Kim, M. J.; Yang, D.; Xie, Z.; Xia, Y. *J. Am. Chem. Soc.* **2011**, *133* (15), 6078–6089.
(20) Lim, B.; Wang, J.; Camargo, P. H. C.; Cobley, C. M.; Kim, M. J.; Xia, Y. *Angew. Chem., Int. Ed.* **2009**, *48* (34), 6304–6308.
(21) Mazumder, V.; Sun, S. H. *J. Am. Chem. Soc.* **2009**, *131* (13), 4588–4589.
(22) Wang, C.; van der Vliet, D.; More, K. L.; Zaluzec, N. J.; Peng, S.; Sun, S.; Daimon, H.; Wang, G.; Greeley, J.; Pearson, J.; Paulikas, A. P.; Karapetrov, G.; Strmcnik, D.; Markovic, N. M.; Stamenkovic, V. R. *Nano Lett.* **2011**, *11* (3), 919–926.
(23) Woods, R. In *Electroanalytical Chemistry*; Bard, A. J., Ed.; Marcel Dekker: New York, 1976; Vol. 9.
(24) Gasteiger, H. A.; Kocha, S. S.; Sompalli, B.; Wagner, F. T. *Appl. Catal., B* **2005**, *56* (1−2), 9–35.
(25) Zhang, J.; Sasaki, K.; Sutter, E.; Adzic, R. R. *Science* **2007**, *315* (5809), 220–222.
(26) Lim, B.; Jiang, M.; Camargo, P. H. C.; Cho, E. C.; Tao, J.; Lu, X.; Zhu, Y.; Xia, Y. *Science* **2009**, *324* (5932), 1302–1305.